Desalination and Water Treatment
www.deswater.com

doi: 10.5004/dwt.2019.23770

151 (2019) 251–263
May

Efficient removal of Pb^{2+} from water using Fe_3O_4@UiO-66-NH_2 core/shell nanocomposite

Sheng Feng*, Shuguang Liu, Shanshan Feng*, Runbai Wang

School of Environmental and Safety Engineering, Changzhou University, Jiangsu 213164, China, Tel. +86-519-86330080; emails: shfeng@cczu.edu.cn (Sheng Feng), fss728@163.com (Shanshan Feng), shguangliu@163.com (Shuguang Liu), ruibaiwang@163.com (Runbai Wang)

Received 12 July 2018; Accepted 10 January 2019

ABSTRACT

Using solvothermal method to combine Amino-functionalized metal–organic frameworks (MOFs) with magnetite (Fe_3O_4 NPS), and the generated magnetic nanocomposite dispersed in MOFs precursor in a row, generating two assembly cycles Fe_3O_4@UiO-66-NH_2 core/shell nanocomposite for efficient removal of Pb^{2+} from aqueous solution. The nanocomposite was characterized by X-ray diffraction (XRD), fourier transform infrared spectra (FT-IR), scanning electron microscopy (SEM), transmission electron microscopy (TEM), nitrogen adsorption-desorption and vibrating sample magnetometer (VSM). Compare the adsorption performance of primary and secondary growth. Batch experiments show that the secondary magnetization of Fe_3O_4@UiO-66-NH_2-2 core/shell nanocomposite has a good removal effect on Pb^{2+}. The prepared Fe_3O_4@UiO-66-NH_2-2 core/shell nanocomposite showed excellent efficient removal of Pb^{2+} with high adsorption capacity (q_e: 19.8 mg·g^{-1}, c_0: 5 mg·L^{-1}) and rapid separation from water by an external magnetic field because of the efficient combination of the advantages of UiO-66-NH_2 and the Fe_3O_4 NPS. The adsorption mechanism is mainly confirmed by the coordination interaction between amino (-NH_2) and Pb^{2+}. These results proved that the preparation of Fe_3O_4@UiO-66-NH_2-2 core/shell nanocomposite can be used as an efficient, separable adsorbent to adsorb Pb^{2+} contaminants in water.

Keywords: UiO-66-NH_2; Fe_3O_4 NPS; Adsorption; Lead ion; Magnetic separation

1. Introduction

Environmental and human threats posed in the environment by highly toxic heavy metal ions continue to be a serious problem because they are not biodegradable and carcinogenic to humans [1]. Sources of heavy metals contaminated wastewater include battery manufacturing, mining, petrochemicals, agrochemicals, fertilizers industries, leather tanning, metal plating, fertilizers industries, ceramic, and glass manufacturing, production of lead additives for gasoline and chemical manufacturing [2,3]. Among the different harmful heavy metals, lead is recognized as one of the most toxic elements, even at low concentrations. According to the US Agency for disease registry and toxic substances, lead is ranked second in the list of prioritized hazardous elements [4]. Lead ion, Pb^{2+}, is no biodegradable and can cause acute and chronic poisoning effects and targets almost of the organs in the human body (the central nervous system is the most affected), heart disease, permanent brain damage, cancer, and even death [5,6]. It is imperative to develop techniques for trapping heavy metals from water [7–11].

Numerous methods have been used for the removal of Pb^{2+}, mainly including adsorption, ion exchange, chemical precipitation, membrane filtration, coagulation–flocculation, and biological method. Among them, the ion exchange method has good selectivity, but the cycle is long. The chemical precipitation method is economical, but the operation is cumbersome. Membrane filtration is highly stable but expensive.

* Corresponding authors.

The coagulation flocculation method has a high recovery rate, but is prone to secondary pollution. The biological method is environmental friendly and low in cost, but the treatment effect is not good [12,13]. At present, biological mediation has become the most promising method for dealing with various pollutants because of its low cost and low environmental pollution. However, it is not very effective in removing Pb^{2+}, because Pb^{2+} can only be adsorbed or adsorbed to biomass but not further degraded by biomass [14,15]. Therefore, adsorption is still an irreplaceable method in Pb^{2+} removal, which is simple in operation, low in cost, and easy to recycle. Traditional adsorbents such as activated carbons suffer from low adsorption capacities [16], and the lack of functional tenability [17], there are urgent needs for the development of new effective adsorbents.

Amino-functionalized metal–organic frameworks (MOFs) are crystalline porous materials. They have attracted much attention because of their characteristics such as well-defined porosities, high surface areas, and chemical stabilities [18,19]. MOFs are promising materials for various technological applications, including gas storage [20], separation [21], drug delivery [22], and chemical sensing [22]. Moreover, MOFs can be functionalized, and this makes them versatile adsorbents. [23,24] The removal of Pb^{2+} in water by amino-functionalized Cr-MOF and the removal of Hg (II) by thiol-functionalized Cu-MOF show the advantages of high adsorption capacity of MOFs [25,26]. Magnetite (Fe_3O_4 NPS) has the advantage of small size and large surface area [27]. It is widely used in immobilized enzyme carrier biochemical products separation, catalysis and other fields [28].

Currently, nanocomposites are favored for their unique application in the removal of water from pollution [15,29–31]. In particular, magnetic nanocomposites are used in wastewater treatment. Due to their unique advantages, polymers can provide favorable functional groups, and the adsorbent can be quickly separated by externally adding a magnetic field [32–34]. Research on composite materials has become one of the areas of best prospects and attractiveness.

As shown in Fig. 1, UiO-66-NH_2 was gradually grown on the surface of Fe_3O_4 NPS by cyclic preparation to generate magnetic Fe_3O_4@UiO-66-NH_2-n (n is the number of assembly cycles) core/shell nanocomposite to removal efficiency of Pb^{2+}. Due to the difficulty of magnetic separation after three successive stages of growth, only one and two graded growths have been studied. The novelty of this work is formed using Fe_3O_4 NPS as the core UiO-66-NH_2 shell in that chemical property of UiO-66-NH_2 is very stable, the prepared material not only avoid the influence of external factors on the stability of the adsorbent, but also quickly and effectively, separated under external magnetic field conditions to avoid secondary pollution. Pb^{2+} can be adsorbed rapidly because amino groups (-NH_2) have lone pair electrons and act as the Lewis base, they can form coordinate bonds with the heavy metal ions (Lewis acids) [35]. The electron-accepting ability of the Lewis acids can be controlled by pH adjustment [36]. After the secondary growth, the increase in the proportion of UiO-66-NH_2 leads to an increase in the surface active sites of the adsorbent, allowing Pb^{2+} to be adsorbed more rapidly. Temperature, pH, and initial ions concentration on the adsorption of Pb^{2+} onto the Fe_3O_4@UiO-66-NH_2 core/shell nanocomposite was carefully investigated. In addition, the excellent removal performance and easy separation of magnetic Fe_3O_4@UiO-66-NH_2 core/shell nanocomposite in wastewater further highlighted its huge potential in environmental remediation applications. On this basis, an effective method is developed to remove Pb^{2+}.

2. Experimental methods

2.1. Materials

All reagents were purchased from Sinopharm Chemical Reagent CO., Ltd, China and used without further purification. They included zirconium chloride ($ZrCl_4$), 2-amino-1,4-benzenedicarboxylate (NH_2-H_2BDC), Iron chloride hexahydrate ($FeCl_3{\cdot}6H_2O$) ethylene glycol, N,N-dimethylformamide (DMF), sodium hydroxide (NaOH), hydrochloric acid (HCl), anhydrous methanol and Lead nitrate. Deionized water was used in the synthesis and all treatment processes.

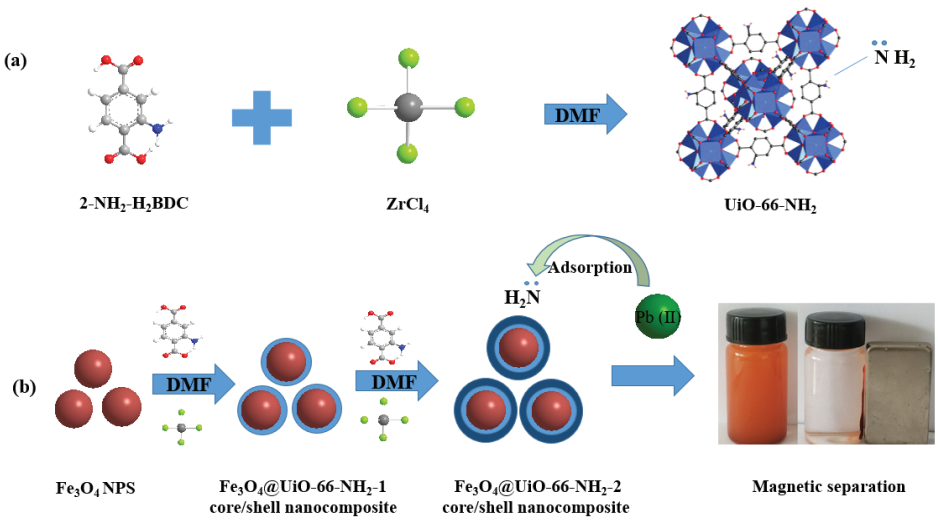

Fig. 1. Schematic illustration of the synthesis of the UiO-66-NH_2 (a), Fe_3O_4@UiO-66-NH_2 core/shell nanocomposite and magnetic separations (b).

2.2. Preparation of Fe_3O_4@UiO-66-NH_2 core/shell nanocomposite

Fe_3O_4 NPS was synthesized according to a literature method with slight modifications [37]. 3.24 g of FeCl3·6H2O was added to 120 mL of ethylene glycol to completely dissolve at room temperature, and then added 1.152 g PAA, 9 ml of deionized water and 7.2 g of urea, ultrasonic for 10 min, transferred to a 200 mL reaction kettle, and reacted at 200°C for 12 h. Magnetic separation, liquid preservation in DMF. UiO-66-NH_2 was prepared by solvating under conventional heating and modified using the reported method [38]. ZrCl4 (0.0848 g, 0.363 mmol) and NH_2-H_2BDC (0.0603 g, 0.363 mmol) in DMF (42 mL) with ultrasonic vibration for 30 min. The as-obtained mixture was transferred to a stainless steel Teflon-lined autoclave of 50 mL capacity and then maintained at 393 K for 24 h. After this time, the autoclave was cooled in air to room temperature and the resulting solid was filtered, repeatedly washed with methanol and dried at room temperature. The magnetic Fe_3O_4@UiO-66-NH_2 core/shell nanocomposite was prepared by a cyclic growth method. First, 0.25 g of Fe_3O_4 NPS was dissolved in 50 mL of DMF and was observed by ultrasonography for 30 min. Subsequently, 0.386 g (1.67 mmol) of ZrCl4 and 0.276 g (1.67 mmol) of NH_2-H_2BDC were added to 50 mL of DMF, and ultrasonically dispersed for 30 min. The two were then mixed and ultrasonication continued for 10 min. The mixed solution was transferred to a 200 mL reaction kettle and heated at 393 K for 24 h. The resulting solution was cooled to room temperature and rapidly separated by external addition of a magnetic field. In the next step, disperse the prepared material in precursors in DMF solutions containing UiO-66-NH_2 precursor. After one to two growth cycles, the samples were collected magnetically, washed with methanol, and dried under vacuum at 100°C. The nanocomposite results are expressed as Fe_3O_4@UiO-66-NH_2-n, where n is the number of assembly cycles.

2.3. Analytical methods

The concentrations of Pb^{2+} were determined by atomic absorption spectroscopy (AAS, Beijing Beifen-Ruili Analytical Instrument Co., Ltd., WFX-130A) during the adsorption process. 0.01 g of the adsorbent was added to a 50 mL initial concentration of Pb^{2+} solution, and the plate was shaken at 200 r·min^{-1} for 6 h using a constant-temperature shaker. The adsorption temperature was 303 K, and the pH of the solution was adjusted to 2 to 6 with dilute hydrochloric acid or sodium hydroxide, respectively. The concentration of adsorbed Pb^{2+} was measured after magnetic separation. In order to obtain the adsorption isotherms of the Pb^{2+}, solutions with varying initial concentration of Pb^{2+} were treated with the same procedure as above at room temperature. Adsorption calculation formula:

$$q_e = \frac{(c_0 - c_e)}{m} \times V \quad (1)$$

where q_e (mg·g^{-1}) is the amount adsorbed per gram of adsorbent, c_0 and c_e are the initial and equilibrium concentrations of Pb^{2+} in the solution (mg·L^{-1}), respectively, m is the mass of the adsorbent used (g), and V (L) is the initial volume of the Pb^{2+} solution.

2.4. Characterization

The powder X-ray diffraction (XRD) measurements were recorded on a Rigaku Dmax/Ultima IV diffractometer (Rigaku, Japan) with monochromatized Cu Kα_1 radiation (λ = 0.15418 nm). Fourier transform infra-red (FTIR) spectra were taken with a Spectrum One FTIR spectrophotometer (Perkin-Elmer, USA) at room temperature. The morphology was observed with a ZEISS Supra 55 microscope (SEM-EDS). The microstructure of the sample was observed by transmission electron microscopy (TEM) (JEM–2100, JEOL, Japan) N_2 adsorption isotherms were obtained using a Micromeritics ASAP 2020 instrument (Micromeritics, USA). The samples were outgassed at 120°C for 8 h before measurement, the specific surface area was calculated by the Brunauere-Emmette-Teller (BET) method. Magnetization measurements were carried out using a vibrating sample magnetometer (VSM, 7404, Lake Shore, an applied magnetic field of 300 Oe at room temperature) under applied magnetic field at room temperature.

3. Results and discussion

3.1. Characterization of Fe_3O_4@UiO-66-NH_2 core/shell nanocomposite

The XRD patterns of the as prepared samples were analyzed by X-ray diffractometer as depicted Fig. 2(a). The Fe_3O_4

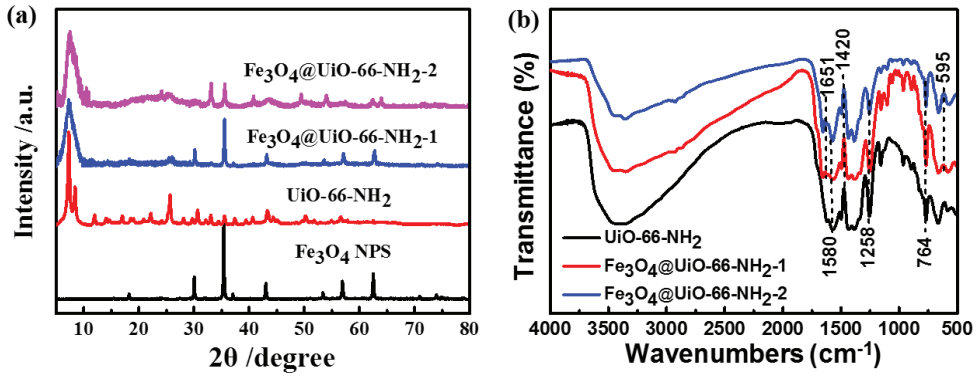

Fig. 2. (a) X-ray diffraction patterns of Fe_3O_4 NPS, UiO-66-NH_2, Fe_3O_4@UiO-66-NH_2-1 and Fe_3O_4@UiO-66-NH_2-2 core/shell nanocomposite; (b) FT-IR patterns of UiO-66-NH_2, Fe_3O_4@UiO-66-NH_2-1 and Fe_3O_4@UiO-66-NH_2-2 core/shell nanocomposite.

NPS pattern had intense reflections at 2θ = 30.1°, 35.5°, 43.1°, 53.4°, and 57.0°, these are typical of Fe_3O_4 NPS respectively [39,40]. Fe_3O_4@UiO-66-NH_2 core/shell nanocomposite was prepared using one or two cycles had additional intense reflections at 2θ between 5° to 60°, which are typical of UiO-66-NH_2 and confirm the formation of highly crystalline UiO-66-NH_2 on the magnetic nanoparticles [41,42]. The corresponding peak has changed after the second growth, due to the difference in the composition ratio of UiO-66-NH_2 and Fe_3O_4 NPS. The simultaneous existence of the characteristic peaks of Fe_3O_4 NPS and UiO-66 in the XRD pattern of Fe_3O_4@UiO-66-NH_2 indicated the successful formation of a UiO-66 shell on the surface of Fe_3O_4 NPS without altering their crystallinity [37].

The infrared spectrum data of the samples are given in Fig. 2(b). There were some absorption peaks in the infrared spectra of UiO-66-NH_2 which come from the aromatic rings and carboxyl groups. For example, the peak at 1,420 cm^{-1} was attributed to the C–C vibrational mode, and the peak at 1,580 cm^{-1} was the stretching vibration of the C–O bond in the carboxyl group [43]. For Fe_3O_4@UiO-66-NH_2, the C–N stretching band and N–H rocking vibration were present at 1,258 and 764 cm^{-1}, the intensity of these bands indicates that as the number of cycles increases, the concentration of -NH_2 groups in the Fe_3O_4@UiO-66-NH_2 core/shell nanocomposite also increases. These FTIR results confirm the presence of an NH2 group in the adsorbents. Simultaneously, combining the characteristic peaks of Fe_3O_4 NPS at 1,651 and 595 cm^{-1} indicates successful synthesis of Fe_3O_4@UiO-66-NH_2 core/shell nanocomposite [37].

In order to investigate the morphology of the products, scanning electron microscopy (SEM) analysis and transmission electron microscopy (TEM) analysis were used. Fig. 3(a) shows a typical morphology of the UiO-66-NH_2. It can be

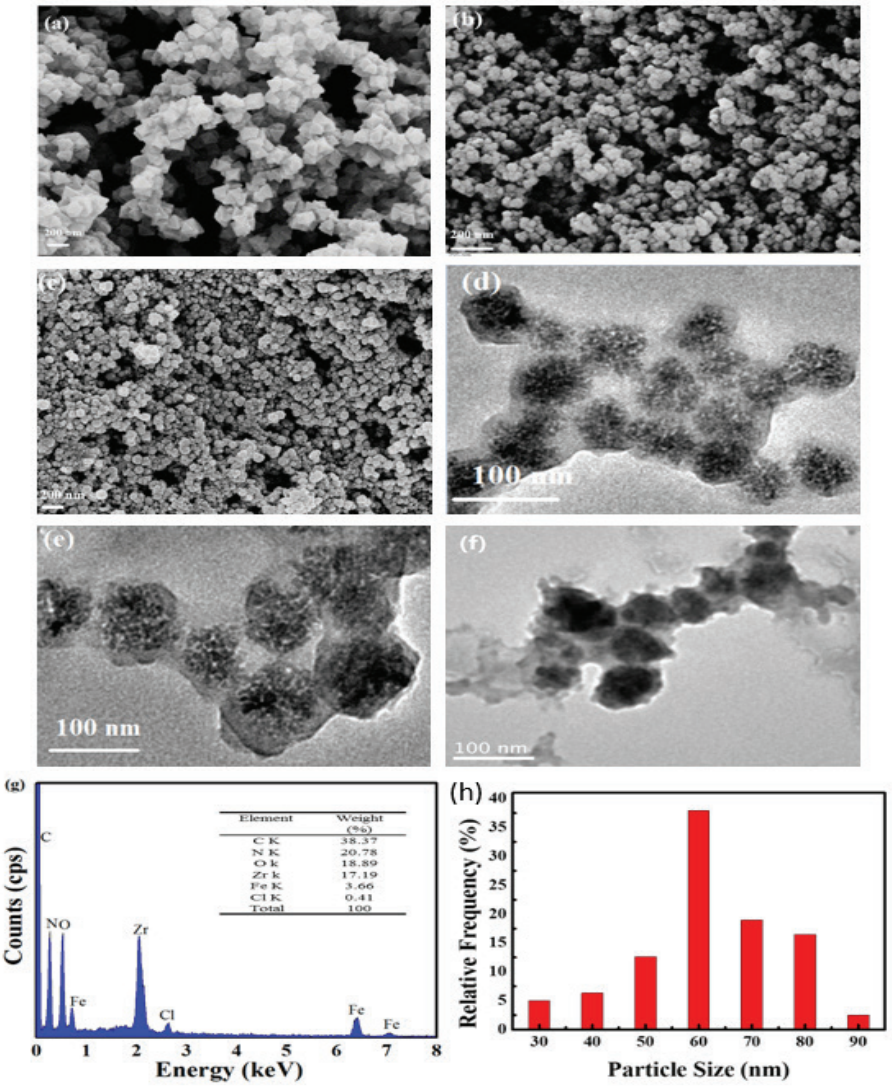

Fig. 3. SEM images of the UiO-66-NH_2 (a), Fe_3O_4@UiO-66-NH_2-1 (b) and Fe_3O_4@UiO-66-NH_2-2 core/shell nanocomposite (c), TEM images of the Fe_3O_4@UiO-66-NH_2-1 (d) and Fe_3O_4@UiO-66-NH_2-2 core/shell nanocomposite (e), adsorbed of Fe_3O_4@UiO-66-NH_2-2 core/shell nanocomposite (f), FESEM-EDS of Fe_3O_4@UiO-66-NH_2-2 core/shell nanocomposite (g), diameter distribution histograms of Fe_3O_4@UiO-66-NH_2-2 (h).

seen that its surface is smooth and has a regular structure. From Fig. 3(b) and (c), representative SEM images shows that the prepared Fe_3O_4@UiO-66-NH_2-2 core/shell nanocomposite was spherical and had narrow size distributions in that UiO-66-NH_2 is uniformly distributed on the surface of Fe_3O_4 NPS. The chemical composition of the material can be clearly observed by EDS analysis. The EDS image in Fig. 3(g) consistently determine the presence of C, N, O, Zr, and Fe elements in the Fe_3O_4@UiO-66-NH_2-2 core/shell nanocomposite. As shown in Fig. 3(f), the diameter of Fe_3O_4 NPS in Fe_3O_4@UiO-66-NH_2-2 core/shell nanocomposite was about 60 nm by measuring at least 100 random nanoparticles in the SEM images using software Image J 1.3s. Fe_3O_4 NPS is evenly decorated inside the UiO-66-NH_2 which can effectively protect the stability of the adsorbent. The TEM images of the nanocomposite in Fig. 3(d) and (e) clearly show core-shell structures, with Fe_3O_4 NPS as the core and UiO-66-NH_2 as the shell.

Nitrogen adsorption-desorption isotherms were applied to verify the porous structures of the materials and to calculate their surface areas and pore volumes. From Fig. 4(a), the UiO-66-NH_2 isotherm belongs to type I, indicating the presence of micropores in the structure, and the process is Langmuir monolayer adsorption [44]. Obviously, the Fe_3O_4@UiO-66-NH_2 core/shell nanocomposite and Fe_3O_4 NPS samples gave adsorption-desorption isotherms intermediate between type I and type IV. The results shown the copresence of micropores and mesopores in the materials [39,40]. The BET surface areas and pore volumes are summarized in Table 1. From Table, the surface areas and pore volumes of Fe_3O_4@UiO-66-NH_2-n increased with increasing number of assembly cycles, this is due to the increase in the proportion of UiO-66-NH_2. After the second growth, the surface area porosity is reduced compared with the original UiO-66-NH_2.

Direct evidence for the formation of Fe_3O_4@UiO-66-NH_2 core/shell nanocomposite was provided using a vibrating sample magnetometer (VSM) at room temperature with an applied magnetic field of 300 kOe [45]. As shown in the Fig. 3(b), the saturation of Fe_3O_4 NPS is 66.83 emu·g–1, the saturation magnetization of Fe_3O_4@UiO-66-NH_2-1 is 39.21 emu·g–1, and the saturation magnetization of Fe_3O_4@UiO-66-NH_2-2 is 27.73 emu·g–1. Although the magnetic strength of Fe_3O_4@UiO-66-NH_2 core/shell nanocomposite is significantly lower than that of Fe_3O_4 NPS, Fe_3O_4@UiO-66-NH_2 core/shell nanocomposite is easily collected by the magnetic field. In Fig. 4(b), the value of remanence magnetization and coercivity of the Fe_3O_4@UiO-66-NH_2 core/shell nanocomposite was very low, declared that they have superparamagnetic at room temperature. The superparamagnetic performances that Fe_3O_4@UiO-66-NH_2 core/shell nanocomposite can be easily separated from water by an applied magnetic field as demonstrated. Meanwhile, after removing the magnetic field, this magnetic nanocomposite can be well dispersed into reaction solution.

3.2. Effect of concentration

Fig. 5 shows the effect of initial concentration of Pb^{2+} on the adsorption capacity of UiO-66-NH_2, Fe_3O_4@UiO-66-NH_2-1 and Fe_3O_4@UiO-66-NH_2-2 core/shell nanocomposite. At different initial concentrations, the adsorption capacity of Fe_3O_4@UiO-66-NH_2-2 core/shell nanocomposite is significantly higher than that of Fe_3O_4@UiO-66-NH_2-1core/shell nanocomposite. With the increase of Pb^{2+} concentration from 5 to 40 mg·L^{-1}, the adsorption capacity of Fe_3O_4@UiO-66-NH_2 core/shell nanocomposite to Pb^{2+} increased rapidly. Due to the low concentration, the adsorption did not reach saturation. As the concentration increases, more power can be provided to overcome the mass transfer resistance of Pb^{2+} from the liquid phase to the adsorbent surface, so that the adsorption capacity becomes larger. When adsorption reaches equilibrium, the adsorption capacity tends to be constant.

Table 1
Parameters of porous structure for UiO-66-NH_2, Fe_3O_4@UiO-66-NH_2-1 and Fe_3O_4@UiO-66-NH_2-2 core/shell nanocomposite

Sample	S_{BET} (m^2/g)	V_t (cm^3/g)	V_{mic} (cm^3/g)	V_{mic}/V_t (%)
Fe_3O_4 NPS	40	0.191	0.181	95
UiO-66-NH_2	729	0.390	0.340	87
UiO-66-NH_2/Fe_3O_4-1	284	0.351	0.077	22
UiO-66-NH_2/Fe_3O_4-2	481	0.496	0.057	11

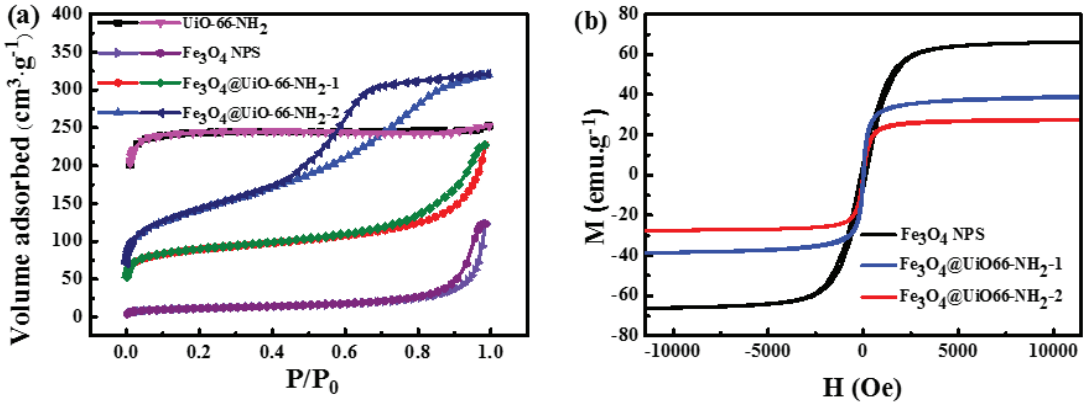

Fig. 4. (a) N_2 adsorption/desorption isotherms of Fe_3O_4 NPS, UiO-66-NH_2, Fe_3O_4@UiO-66-NH_2-1 a Fe_3O_4@UiO-66-NH_2-2 core/shell nanocomposite; (b) Magnetization hysteresis curves of Fe_3O_4, Fe_3O_4@UiO-66-NH_2-1 and Fe_3O_4@UiO-66-NH_2-2 core/shell nanocomposite.

3.3. Effect of contact time

Fig. 6 illustrates the effect of contact time on adsorbent removal Pb^{2+}. Adsorption is significantly faster in 60 min, the Fe_3O_4@UiO-66-NH_2-1 core/shell nanocomposite on Pb^{2+} was 13.2 mg·g^{-1}, the removal rate was 52.8%. The adsorption of Fe_3O_4@UiO-66-NH_2-2 core/shell nanocomposite on Pb^{2+} was 14.3 mg·g^{-1} and the removal rate was 57.3%. Obviously, it can be seen that the amount of adsorption of secondary growth is significantly higher than that of primary growth which due to the completely amino-functionalized structure resulting in rapid migration of heavy metal ions into the adsorbent. The amount of adsorption gradually increases with increasing of time and adsorption equilibrium was established after 2 h. In the end, the adsorption amount of both adsorbents reached 16.3and 18.6 mg·g^{-1}.

3.4. Effect of pH

As depicted in Fig. 7, the pH has a great effect on the adsorption capacity of Pb^{2+} on the Fe_3O_4@UiO-66-NH_2 core/shell nanocomposite. Insoluble matter that does not produce $Pb(OH)_2$ at pH < 6, respectively [46]. Moreover, the structure of the MOFs in water is highly stable especially in acidic environments [43]. Hence, the pH values in the range of 2 to 6 were chosen. It can be seen from the figure that the pH value had a significant influence on the adsorption capacity of the NH_2 functionalized adsorbent. When the pH is 2, the adsorption amount of Fe_3O_4@UiO-66-NH_2-1 core/shell nanocomposite to Pb^{2+} is 3.1 mg·g^{-1}, and the adsorption of Fe_3O_4@UiO-66-NH_2-2 core/shell nanocomposite to Pb^{2+} is 4.2 mg·g^{-1}. With the increase of pH, the adsorption amount gradually increases, when pH 6 was reached, the adsorption of Pb^{2+} on the two adsorbents gradually reached 15.9 and 18.2 mg·g^{-1}, adsorption capacity for secondary growth is always higher than primary growth. Such a pH dependent sorption may be rationalized based on the surface charge of the sorbents. When the pH is low, the active sites on the sorbents are protonated and positively charged, the positively charged Pb^{2+} ions are not favored by the positively charged active sites due to the electrostatic repulsive effect, leading to a lower sorption capacity. At higher pH, the active site become deprotonated and the electrostatic repulsion between the group and the Pb^{2+} ion decreases or even disappears. The coordination or hydrogen bonds interaction incites an increase of the sorption capacity. On the other hand, pH induced Pb^{2+} speciation may also be responsible for the pH dependent sorption [47]. In consideration of high adsorption capacity, the pH of 6 was a proper value. On the contrary, lower pH is beneficial to desorption.

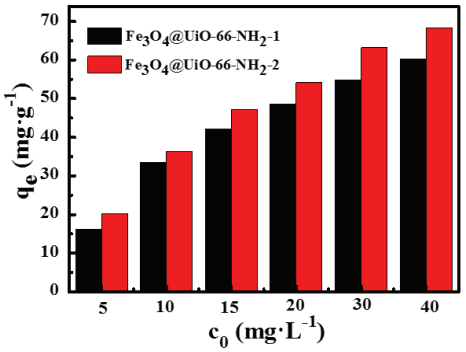

Fig. 5 Effect of concentration for Pb^{2+} adsorption on Fe_3O_4@UiO-66-NH_2-1 and Fe_3O_4@UiO-66-NH_2-2 core/shell nanocomposite. (T = 303 K; m = 10 mg; V = 50 mL; pH = 6).

3.5. Adsorption kinetics

In this work, adsorbent Fe_3O_4@UiO-66-NH_2-2 core/shell nanocomposite was further studied in the Pb^{2+} adsorption process to better explain the excellent adsorption performance and adsorption mechanism of the adsorbent.

To better understand the adsorption mechanism and kinetics, the pseudo-first-order, pseudo-second-order and intra-particle diffusion kinetic models were used to investigate the kinetics of Pb^{2+} adsorption on the Fe_3O_4@UiO-66-NH_2-2 core/shell nanocomposite. The model is as follows [48–50].

$$\ln(q_e - q_t) = \ln q_e - kt \tag{2}$$

$$\frac{t}{q_t} = \frac{1}{k_2 q_2^2} + \frac{t}{q_2} \tag{3}$$

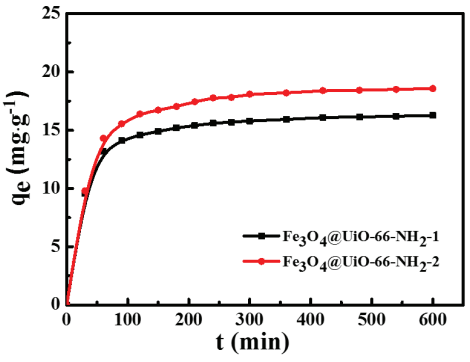

Fig. 6. Time profile of Pb^{2+} adsorption on the Fe_3O_4@UiO-66-NH_2-1 and Fe_3O_4@UiO-66-NH_2-2 core/shell nanocomposite. (T = 303 K; m = 10 mg; V - 50 mL; pH = 6).

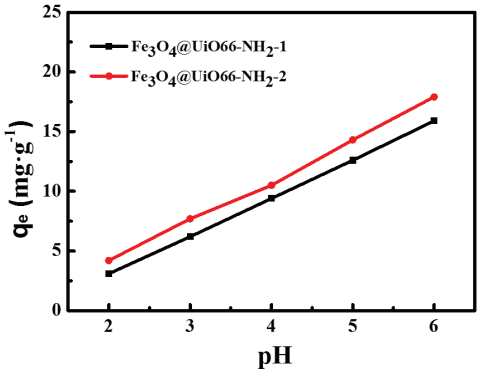

Fig. 7. Effect of solution pH on the adsorption on the Fe_3O_4@UiO-66-NH_2-1 and Fe_3O_4@UiO-66-NH_2-2 core/shell nanocomposite. (c_0 = 5 mg·L^{-1}; T = 303 K; t = 6 h; m = 10 mg; V = 50 mL).

$$q_t = \beta \ln(\alpha\beta) + \beta \ln t \quad (4)$$

where t is the adsorption time (min), q_t is the amount of adsorption at time t (mg·g^{-1}). q_e and q_2 are the equilibrium adsorption capacities (mg·g^{-1}) for the first-order kinetic model and the quasi-second-order kinetic model. k_1 primary reaction rate constant (min^{-1}), k_2 is the quasi-secondary reaction rate constant, where α and β are the Elovich constants and represent the initial adsorption rate (g·mg^{-1} min^{-1}) and the desorption constant (mg·g–$^{-1}$·min^{-1}), respectively. The Elovich constants can be obtained from the graphs of q_t vs. lnt.

Table 2 and Figs. 8(a), (b), and (c) shows the results of quasi-first-order, quasi-second-order kinetic model, and Elovich kinetic model for the adsorption of Pb^{2+} by Fe_3O_4@UiO-66-NH_2-2 core/shell nanocomposite, the quasi-second-order kinetic linear correlation coefficient, the theoretical equilibrium adsorption capacity and the experimental results. It can be seen that the pseudo-second-order kinetic model is more suitable for the explanation of the Pb^{2+} adsorption mechanism because the relationship between experimental data and kinetics is determined by applying the correlation coefficient (R^2), and the pseudo-second-order kinetics R^2 value is higher than Pseudo-first-order kinetics and Elovich models. In addition, the calculated q_e value is also consistent with the experimental data. In addition, the calculated q_e value is also consistent with the experimental data. Therefore, the adsorption of Pb^{2+} by magnetic materials conforms to the pseudo-second-order kinetic equation.

The adsorption kinetics of Pb^{2+} solid particles are controlled by the following three steps: (1) boundary diffusion, (2) Pb^{2+} adsorption on the surface of solid particles, (3) internal diffusion [51]. The internal diffusion model is as follows:

$$q_e = k_p t^{0.5} + B \quad (5)$$

k_p (mg·g^{-1}·min$^{0.5}$) is the particle diffusion rate constant. B is the adsorption constant. If the multi–linearity is plotted with $q_e - t^{0.5}$, it indicates that the adsorption process is a complex

Table 2
Fe_3O_4@UiO-66-NH_2-2 core/shell nanocomposite adsorption of Pb^{2+} kinetic parameters

	Pseudo-first-order kinetics			Pseudo-second-order kinetics			Elovich		
T/K	$k_1 \times 10^2$ min^{-1}	$q_{e\text{-cal}}$ mg·g^{-1}	R^2	$k_2 \times 10^{-4}$ g·(mg·min)$^{-1}$	$q_{e\text{-cal}}$ mg·g^{-1}	R^2	α	β	R^2
293	1.400	14.89	0.975	12.063	18.09	0.999	0.082	3.779	0.982
303	1.080	8.83	0.974	17.794	19.83	0.999	0.264	3.385	0.916
313	1.090	9.36	0.975	19.438	18.85	0.999	0.189	3.373	0.931

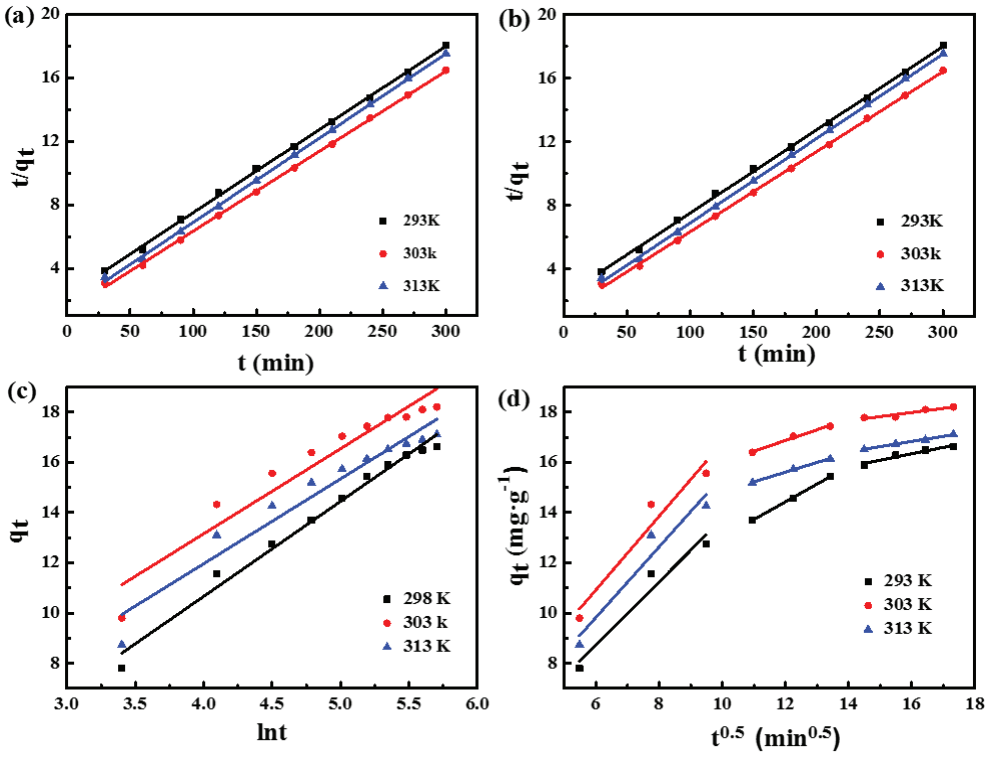

Fig. 8. Pseudo-first-order kinetic model (a), pseudo-second-order kinetic model (b), Elovich kinetic model (c) and intraparticle diffusion kinetic model (d) for the adsorption of Pb^{2+} on Fe_3O_4@UiO-66-NH_2-2 core/shell nanocomposite with different temperature.

process controlled by multiple velocity steps. If a straight line is obtained, the entire adsorption process is controlled by the diffusion inside the particles, and if it is straight and through the origin, it is the only constant speed step. As shown in Fig. 7(d), the kinetic data were fitted with three-stage linearity by intra–particle diffusion model, indicating that the adsorption process is complex, which is divided into three stages: the adsorption of Pb^{2+} on the first stage adsorbent increases with $t^{0.5}$ and significantly increased, which corresponds to the diffusion of the boundary layer of Pb^{2+}. In the second stage, the adsorption of Pb^{2+} on the adsorbent increases with the increase of $t^{0.5}$, but the slope of the second line is smaller and the adsorption capacity increases more slowly than the first stage, because the second stage controlled by particle diffusion. The third stage of adsorption tends to saturate, which means that the adsorption reaches equilibrium stage. Therefore, the process of adsorption Pb^{2+} was not only controlled by the in-particle diffusion, but also by the membrane diffusion.

3.6. Adsorption isotherm

The adsorption behavior of Fe_3O_4@UiO-66-NH_2-2 core/shell nanocomposite on Pb2+ was simulated by Langmuir, Freundlich, and Tempkin adsorption models. The model is as follows [52–54]:

$$\frac{c_e}{q_e} = \frac{1}{Q_m K_L} + \frac{c_e}{Q_m} \tag{6}$$

$$\ln q_e = \ln K_F + \frac{\ln c_e}{n} \tag{7}$$

$$q_e = B\ln K_T + B\ln c_e \tag{8}$$

where c_e (mg·L^{-1}) is the equilibrium concentration of Pb^{2+}. q_e (mg·g^{-1}) for the amount of adsorbent adsorbed Pb^{2+}. Q_m (mg·g^{-1}) is the maximum adsorption capacity, K_L (L·mg^{-1}) is the balance constant. Where K_F and $1/n$ represents the Freundlich constant of adsorption capacity and adsorption intensity, respectively. B and K_T (L·g^{-1}) are the constant.

Isotherm studies can describe how the adsorbates interact with adsorbents, affording the most important parameter for designing a desired adsorption system. The adsorption isotherms of Pb^{2+} on the Fe_3O_4@UiO-66-NH_2-2 core/shell nanocomposite at different initial concentrations are given in Fig. 9. As shown in Table 3, which summarizes the Langmuir, Freundlich, and Temkin constants and the

Table 3
Langmuir, Freundlich and Temkin parameters for adsorption of Pb^{2+} by Fe_3O_4@UiO-66-NH_2-2 core/shell nanocomposite at different temperature

Isothermal	Parameter	293 K	303 K	313 K
Langmuir equation	Q_m (mg·g^{-1})	68.59	75.41	73.05
	K_L (L·mg^{-1})	0.18	0.33	0.22
	R^2	0.996	0.997	0.995
Freundlich equation	K_F (mg·g^{-1})	8.772	23.240	18.349
	$1/n$	0.428	0.359	0.400
	R^2	0.952	0.943	0.946
Temkin equation	B (L·g^{-1})	14.540	14.542	14.925
	K_T (L·g^{-1})	1.928	4.421	2.592
	R^2	0.992	0.986	0.991

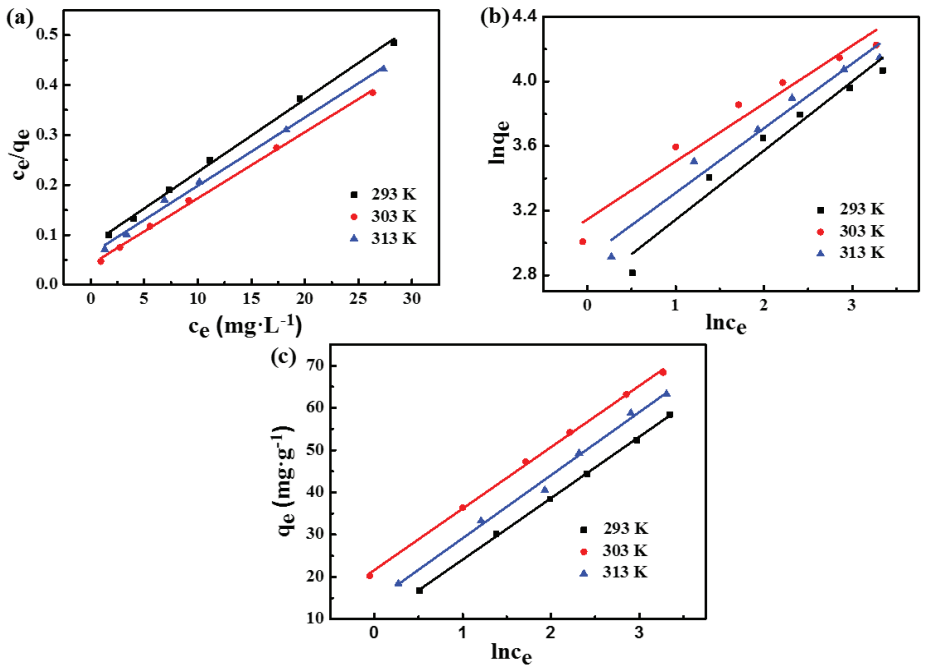

Fig. 9. Langmuir (a), Freundlich (b), and Temkin (c) isotherm model for Pb^{2+} adsorption onto Fe_3O_4@UiO-66-NH_2-2 core/shell nanocomposite at different temperatures.

calculated coefficients the Freundlich equation correlation coefficient of Fe_3O_4@UiO-66-NH_2-2 core/shell nanocomposite adsorbed Pb^{2+} indicates that the adsorption of Pb^{2+} on Fe_3O_4@UiO-66-NH_2-2 core/shell nanocomposite is in agreement with Langmuir. The dsorption of Pb^{2+} on Fe_3O_4@UiO-66-NH_2-2 core/shell nanocomposite is also in agreement with Langmuir.

In order to determine whether an adsorption system is "favorable" or "unfavorable" between the adsorbent and the adsorbate, R_L, the separation factor or equilibrium parameter, is also calculated using Eq. (9) [55].

$$R_L = \frac{1}{1+bc_0} \tag{9}$$

where b (L·mg^{-1}) is the Langmuir constant and c_0 (mg·L^{-1}) is the initial Pb^{2+} concentration. The value of R_L indicates the shape of the isotherm to be either unfavorable ($R_L > 1$), linear ($R_L = 1$), favorable ($0 < R_L < 1$) or irreversible (R_L=0) [56]. The R_L values between 0 and 1 indicate favorable adsorption. For Pb^{2+} adsorption on the Fe_3O_4@UiO-66-NH_2-2 core/shell nanocomposite, the R_L values obtained are far less than one, thereby confirming that the adsorption is a favorable process.

3.7. Adsorption thermodynamics

To study the inherent energy changes within the adsorption process, the thermodynamic parameters of the adsorption were investigated. The change in the Gibbs free energy (ΔG), enthalpy (ΔH), and entropy (ΔS) were calculated from the following equations [57]:

$$\Delta G = -RT\ln K_D \tag{10}$$

$$\ln K_D = \frac{\Delta S}{R} - \frac{\Delta H}{RT} \tag{11}$$

where R is the gas constant (8.314 J·mol^{-1}·K^{-1}), K_D is the distribution coefficient ($K_D = q_e/c_e$), ΔH and ΔS can be calculated from the slope of the curve and intercept of the calculated temperature of the adsorption of Pb^{2+} thermodynamic parameters shown in Fig. 10 and Table 4.

When T < 313 K, the negative ΔG can promote the adsorption of Pb^{2+} on Fe_3O_4@UiO-66-NH_2-2 core/shell nanocomposite was carried out spontaneously, the adsorption value was 136.21 and 34.37 kJ·mol^{-1} which is greater than zero and indicates that the degree of confusion in the adsorption process is increased because the adsorption of a large number of water molecules at the solid/liquid interface is greater than zero. When $T \geq 313$ K, the negative values of ΔG confirm the feasibility of the process and spontaneous nature of the adsorption. When ΔH more than 40 kJ·mol^{-1} illustrates that the adsorption process is chemisorption, less than 40 kJ·mol^{-1}, shows that the adsorption process is physical adsorption, 34.47, 14.29 kJ·mol^{-1} are less than 40 kJ·mol^{-1}, launches that the adsorption process is physical adsorption [57]. In all temperatures, the $|\Delta S| > |\Delta H|$, demonstrating that the adsorption is dominated by entropy effect rather than enthalpy change.

3.8. Adsorbent stability

Further investigation of the adsorbent before and after adsorption was conducted in order to elucidate the adsorbent stability. In Fig. 11(a), the XRD comparison of the adsorbent before and after adsorption shows that the peak position is obviously the same, inference that there is no obvious change in the crystal structure of the adsorbent after adsorption. The comparison of FT-IR before and after adsorption was shown in Fig. 11(b), the adsorbent peak position before and after adsorption were the same, and it can be concluded that the functional groups were the same before and after adsorption,

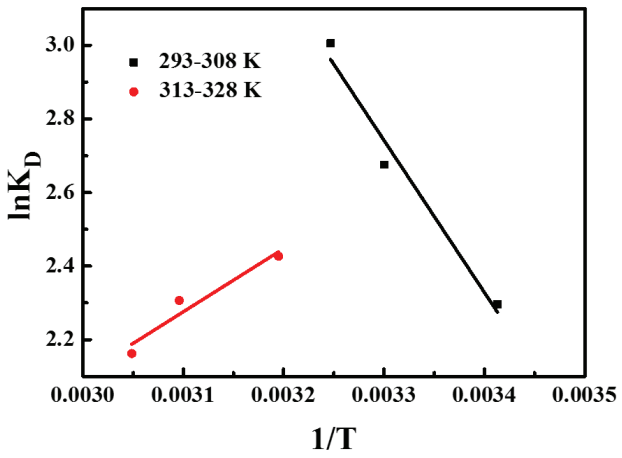

Fig. 10. Plot of $\ln K_D$ vs.1/T for Pb^{2+} dye adsorption by Fe_3O_4@UiO-66-NH_2-2 core/shell nanocomposite. (c_0 = 5 mg·L^{-1}; t = 6 h; m = 10 mg; V = 50 mL).

Table 4
Thermodynamic parameters of Pb^{2+} in Fe_3O_4@UiO-66-NH_2-2 core/shell nanocomposite adsorbed water

Temperature/K	K_D/L·mg^{-1}	ΔG/kJ·mol^{-1}	ΔS/J·(mol·K)$^{-1}$	ΔH/kJ·mol^{-1}
293	9.93	–5.592		
303	14.52	–6.740	136.21	34.37
308	20.20	–7.696		
313	11.32	–6.314		
323	10.04	–6.194	–25.36	14.29
328	8.69	–5.896		

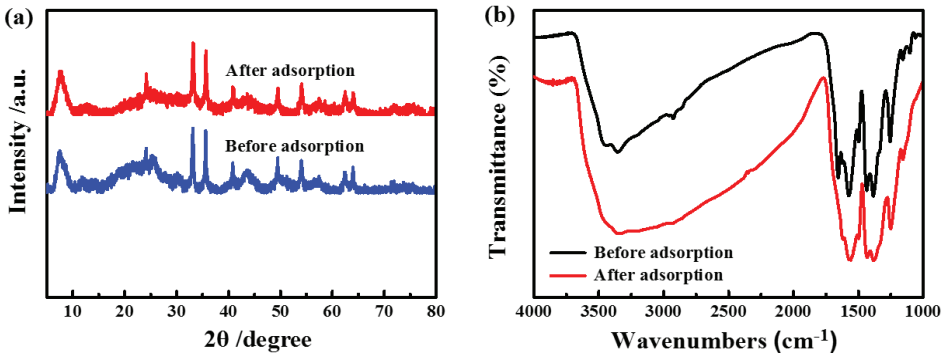

Fig. 11. (a) XRD patterns of Fe_3O_4@UiO-66-NH_2-2 core/shell nanocomposite before (fresh) and after adsorption. (b) FTIR spectra of the Fe_3O_4@UiO-66-NH_2-2 core/shell nanocomposite before (fresh) and after adsorption.

after the adsorption, the earlier mentioned bands decreased due to the coordination of N in the amino group (−NH_2) with Pb^{2+}, consistent with the literature [58] report. The above results confirm that the adsorbent has better stability.

3.9. Comparison with other adsorbents

From Table 5, it can be seen that Fe_3O_4@UiO-66-NH_2-2 core/shell nanocomposite has great potential for Pb^{2+} adsorption. The reasons for this phenomenon is due to the -NH_2 can form coordinate bonds with the heavy metal ions contained in the Fe_3O_4@UiO-66-NH_2-2 core/shell nanocomposite. Compared with the material filtration and separation in Table 5, the material can be quickly separated by an external magnetic field to avoid secondary pollution, moreover, since it is a core-shell structure, Fe_3O_4 NPS is a core, which can avoid corrosion of Fe_3O_4 NPS by the external environment and make the adsorbent more stable. This study provides an easy way to prepare highly efficient magnetic nanomaterial adsorbents to remove Pb^{2+} from water. These advantages are not available in the other materials shown in Table 5.

3.10. Effect of background ions

Coexistent metal ions, such as Cu^{2+}, Cd^{2+}, Cs^{+}, Mg^{2+}, Hg^{2+}, and Al^{3+} are ubiquitous in ambient water and can compete with metal ions Pb^{2+} for the adsorption sites of adsorbents. Therefore, it is important to study the effect on the adsorption behavior in the presence of metal ions. As shown in Fig. 12, when the coexistence of Pb^{2+} and Cu^{2+}, the adsorbent adsorbed Pb^{2+} at a minimum of 13.8 mg·g^{-1}. In the coexistence with Cd^{2+}, the Fe_3O_4@UiO-66-NH_2-2 core/shell nanocomposite amount of Pb^{2+} was up to 17.46 mg·g^{-1} with almost no effect. The results show that the presence of these competing metal ions has little effect on the adsorption of Pb^{2+} by the adsorbent, the good selective removal of Pb^{2+} may be due to the functionalization of NH_2 [66]. Cu^{2+}, Cd^{2+}, Cs^{+}, Mg^{2+}, Hg^{2+}, and Al^{3+} did not significantly compete with Pb^{2+} as an adsorption site for Fe_3O_4@UiO-66-NH_2-2 core/shell nanocomposite.

3.11. Application to real samples

In order to study the using in the actual environment, the removal of Pb^{2+} from Fe_3O_4@UiO-66-NH_2-2 core/shell nanocomposite in actual wastewater was studied in Fig. 13.

Table 5
Comparison of q_e for different adsorbents

Serial number	Adsorbents	q_e/(mg·g^{-1})	References
1	Fe_3O_4@UiO-66-NH_2-2 core/shell nanocomposite	19.83	This study
2	β-MnO_2	13.57	[59]
3	CaAl layered double hydroxides	20.79	[60]
4	Al_2O_3 nanoparticles	29.1	[61]
5	MgAl-LDHs	16.93	[62]
6	Commercial activated carbon	5.95	[63]
7	Commercial granular activated carbon	10.8	[64]
8	MnOx-loaded biochar	86.5	[65]

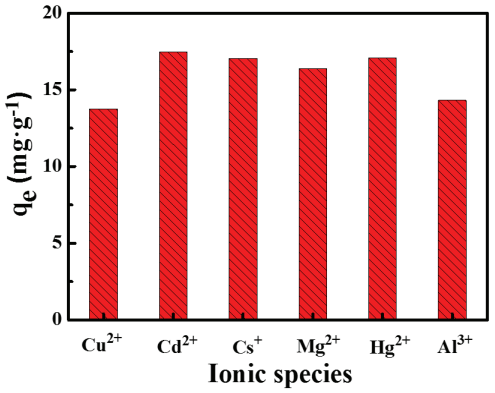

Fig. 12. Effect of coexisting ions on the removal of Pb^{2+} by Fe_3O_4@UiO-66-NH_2-2 core/shell nanocomposite. (c_0 = 5 mg·L^{-1}; t = 6 h; m = 10 mg; V = 50 mL).

Configure Pb^{2+} ion solution with a concentration of 5 mg·L^{-1} (Deionized water, lake water, tap water, and purified water), adsorption capacity for them can reach 18.43, 16.89, 17.43,and 19.47 mg·g^{-1} respectively. The removal efficiency of Pb^{2+} can reach more than 74%. These results show that Fe_3O_4@UiO-66-NH_2-2 core/shell nanocomposite has a significant

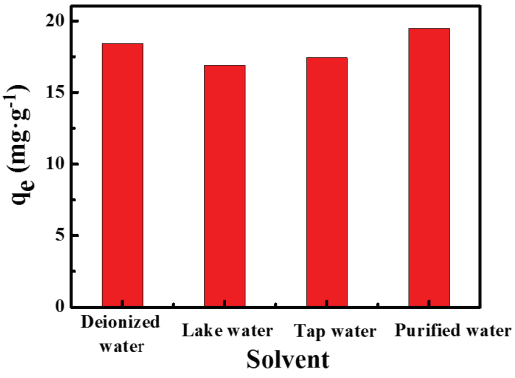

Fig. 13. Adsorption of Pb^{2+} to Fe_3O_4@UiO-66-NH_2-2 core/shell nanocomposite in actual water samples. (c_0 = 5 mg·L^{-1}; t = 6 h; m = 10 mg; V = 50 mL).

effect on the removal of Pb^{2+} from complex wastewater. Therefore, Fe_3O_4@UiO-66-NH_2-2 core/shell nanocomposite is a promising adsorbent for the removal of Pb^{2+}.

4. Conclusions

Fe_3O_4@UiO-66-NH_2-2 core/shell nanocomposite was prepared by two assembly cycles has a clear core-shell structure and has a better adsorption effect on Pb^{2+}. The results showed that the process accorded with quasi-second-order kinetic equations and Freundlich adsorption model. In addition, adsorption thermodynamic parameters indicated that this process was divided into two processes. The magnetic composite has a strong adsorption capacity for Pb^{2+} in water with a saturated adsorption capacity of 19.83 mg g^{-1}. Complementary, the amino groups (−NH_2) have lone pair electrons and act as the Lewis base, they can form coordinate bonds with the heavy metal ions. The electron-accepting ability of the Lewis acids can be controlled by pH, which is the main reason for high adsorption capacity of adsorbent. The stability of the adsorbent indicated that the crystal structure and morphology of the Fe_3O_4@UiO-66-NH_2-2 core/shell nanocomposite do not change significantly after adsorption. The study demonstrated that the prepared Fe_3O_4@UiO-66-NH_2-2 core/shell nanocomposite can be used as magnetically separable and highly efficient adsorbents for removing Pb^{2+} from aqueous solutions.

Acknowledgements

The present research supported by the Natural Science Foundation of China (No. 41371446 and No. 41271498), science and Technology Project of Changzhou University: ZMF17020117, natural science fund for colleges and universities in Jiangsu Province: 18KJB610001 and natural Science Foundation of Jiangsu Province: BK20180964.

References

[1] R.S. Boyd, Heavy metal pollutants and chemical ecology: exploring new frontiers, J. Chem. Ecol., 36 (2010) 46–58.
[2] X.M. Li, W. Zheng, D.B. Wang, Q. Yang, J.B. Cao, X. Yue, T.T. Shen, G.M. Zeng, Removal of Pb (II) from aqueous solutions by adsorption onto modified areca waste: kinetic and thermodynamic studies, Desalination, 258 (2010) 148–153.
[3] M. Momčilović, M. Purenović, A. Bojić, A. Zarubica, M. Ranđelović, Removal of lead(II) ions from aqueous solutions by adsorption onto pine cone activated carbon, Desalination, 276 (2011) 53–59.
[4] D.H.K. Reddy, Y. Harinath, K. Seshaiah, A.V.R. Reddy, Biosorption of Pb(II) from aqueous solutions using chemically modified Moringa oleifera tree leaves, J. Chem. Ecol., 162 (2010) 626–634.
[5] Y. Guo, W.U. Xiao-Yan, W. Xiong, C.Y. Hui, Prevention and treatment of lead poisoning in children A review with recent updates, Child Health Care, 25(2017) 378–381.
[6] G.M. Naja, B. Volesky, 2 Toxicity and sources of Pb, Cd, Hg, Cr, As, and radionuclides in the environment, Health, 13 (2009) 13–62.
[7] F. Fu, L. Xie, B. Tang, Q. Wang, S. Jiang, Application of a novel strategy—Advanced Fenton-chemical precipitation to the treatment of strong stability chelated heavy metal containing wastewater, Chem. Eng. J., 189–190 (2012) 283–287.
[8] Y. Li, L. Wang, X. Yin, B. Ding, G. Sun, T. Ke, J. Chen, J. Yu, Colorimetric strips for visual lead ion recognition utilizing polydiacetylene embedded nanofibers, J. Mater. Chem. A, 2 (2014) 18304–18312.
[9] J. Feng, Z. Yang, G. Zeng, J. Huang, H. Xu, Y. Zhang, S. Wei, L. Wang, The adsorption behavior and mechanism investigation of Pb(II) removal by flocculation using microbial flocculant GA1, Technol., 148 (2013) 414–421.
[10] Q. Zhang, Q. Du, M. Hua, T. Jiao, F. Gao, B. Pan, Sorption enhancement of lead ions from water by surface charged polystyrene-supported nano-zirconium oxide composites, Environ. Sci. Technol., 47 (2013) 6536–6544.
[11] Y. Huang, A.A. Keller, EDTA functionalized magnetic nanoparticle sorbents for cadmium and lead contaminated water treatment, Water Res., 80 (2015) 159–168.
[12] Ihsanullah, A. Abbas, A.M. Al-Amer, T. Laoui, M.J. Al-Marri, M.S. Nasser, M. Khraisheh, M.A. Atieh, Heavy metal removal from aqueous solution by advanced carbon nanotubes: critical review of adsorption applications, Technol., 157 (2016) 141–161.
[13] D. Ghosh, R. Saha, A. Ghosh, R. Nandi, B. Saha, A review on toxic cadmium biosorption from contaminated wastewater, Desalination., 53 (2015) 413–420.
[14] J. Wang, X. Jiang, X. Liu, X. Sun, W. Han, J. Li, L. Wang, J. Shen, Microbial degradation mechanism of pyridine by Paracoccus sp. Njust 30 newly isolated from aerobic granules, Chem. Eng. J., 344 (2018) 86–94.
[15] A. Bozkurt, R. Deumens, C. Beckmann, D.L. Olde, F. Schügner, I. Heschel, B. Sellhaus, J. Weis, W. Jahnendechent, G.A. Brook, In vitro cell alignment obtained with a Schwann cell enriched microstructured nerve guide with longitudinal guidance channels, Biomater., 30 (2009) 169–179.
[16] H. Kim, B.I. Lee, S.H. Byeon, The inner filter effect of Cr(VI) on Tb-doped layered rare earth hydroxychlorides: new fluorescent adsorbents for the simple detection of Cr(VI), Commun., 51 (2015) 725–728.
[17] R-B. Lin, T-Y. Li, H-L. Zhou, C-T. He, J-P. Zhang, X-M. Chen, Tuning fluorocarbon adsorption in new isoreticular porous coordination frameworks for heat tansformation applications, Chem. Sci., 6 (2015) 2516–2521.
[18] Q.L. Zhu, Q. Xu, Metal-organic framework composites, Soc. Rev., 43 (2014) 5468–5512.
[19] O.K. Farha, J.T. Hupp, Rational design, synthesis, purification, and activation of metal–organic framework materials, Chem. Res., 43 (2010) 1166–1175.
[20] G. Li, H. Kobayashi, J.M. Taylor, R. Ikeda, Y. Kubota, K. Kato, M. Takata, T. Yamamoto, S. Toh, S. Matsumura, Hydrogen storage in Pd nanocrystals covered with a metal-organic framework, Nat. Mater., 13 (2014) 802–806.
[21] Z.Y. Gu, C.X. Yang, N. Chang, X.P. Yan, Metal-organic frameworks for analytical chemistry: from sample collection to chromatographic separation, Chem. Res., 45 (2012) 734–745.
[22] P. Horcajada, C. Serre, G. Maurin, N.A. Ramsahye, F. Balas, M. Vallet-Regí, M. Sebban, F. Taulelle, G. Férey, Flexible porous metal-organic frameworks for a controlled drug delivery, J. Amer. Chem. Soc., 130 (2008) 6774–6780.

[23] B. Gole, U. Sanyal, R. Banerjee, P.S. Mukherjee, High loading of Pd nanoparticles by interior functionalization of MOFs for heterogeneous catalysis, Inorg. Chem., 55 (2016) 2345–2354.
[24] L. Qin, Z. Li, Q. Hu, Z. Xu, X. Guo, G. Zhang, One-pot assembly of metal/organic-acid sites on amine-functionalized ligands of MOFs for photocatalytic hydrogen peroxide splitting, Chem. Commun., 52 (2016) 7110–7113.
[25] F. Ke, L.G. Qiu, Y.P. Yuan, F.M. Peng, X. Jiang, A.J. Xie, Y.H. Shen, J.F. Zhu, Thiol-functionalization of metal-organic framework by a facile coordination-based postsynthetic strategy and enhanced removal of Hg^{2+} from water, J. Hazard. Mater., 196 (2011) 36–43.
[26] X. Luo, L. Ding, J. Luo, Adsorptive removal of Pb(II) Ions from aqueous samples with amino-functionalization of metal–organic frameworks MIL-101(Cr), J. Chem. Eng. Data, 60 (2015) 1732–1743.
[27] I. Savva, O. Marinica, C. Papatryfonos, L. Vekas, T. Krasiachristoforou, Evaluation of electrospun polymer-Fe_3O_4 nanocomposite mats in malachite green adsorption, RSC Adv., 5 (2015) 16484–16496.
[28] Y.K. Lv, J. Zhang, M.Z. Li, S.D. Zhou, X.H. Ren, J. Wang, Fast clean-up and selective enrichment of florfenicol in milk by restricted access media molecularly imprinted magnetic microspheres based on surface-initiated photoiniferter-mediated polymerization, Methods, 8 (2016) 3982–3989.
[29] M.M. Lakouraj, F. Mojerlou, E.N. Zare, Nanogel and superparamagnetic nanocomposite based on sodium alginate for sorption of heavy metal ions, Carbohydr. Polym., 106 (2014) 34–41.
[30] E. Nazarzadeh Zare, M. Mansour Lakouraj, P. Najafi Moghadam, R. Hasanzadeh, Novel conducting nanocomposite based on polypyrrole and modified poly(styrene-alt-maleic anhydride) via emulsion polymerization: synthesis, Characterization, Antioxidant, and heavy metal sorbent activity, Polym. Compos., 36 (2015) 138–144.
[31] E.N. Zare, M.M. Lakouraj, Biodegradable polyaniline/dextrin conductive nanocomposites: synthesis, characterization, and study of antioxidant activity and sorption of heavy metal ions, Iranian Polym. J., 23 (2014) 257–266.
[32] M.M. Lakouraj, F. Hasanzadeh, E.N. Zare, Nanogel and super-paramagnetic nanocomposite of thiacalix[4]arene functionalized chitosan: synthesis, characterization and heavy metal sorption, Iranian Polym. J., 23 (2014) 933–945.
[33] E.N. Zare, M.M. Lakouraj, A. Ramezani, Efficient sorption of Pb(II) from an aqueous solution using a poly(aniline-co-3-aminobenzoic acid)-based magnetic core-shell nanocomposite, New J. Chem., 40 (2016) 2521–2529.
[34] R. Hasanzadeh, P.N. Moghadam, N. Bahri-Laleh, M. Sillanpää, Effective removal of toxic metal ions from aqueous solutions: 2-Bifunctional magnetic nanocomposite base on novel reactive PGMA-MAn copolymer@Fe_3O_4 nanoparticles, J. Colloid Interface Sci., 490 (2017) 727–746.
[35] S. Edebali, E. Pehlivan, Evaluation of Cr(III) by ion-exchange resins from aqueous solution: equilibrium, thermodynamics and kinetics, Desalination, 52 (2014) 7143–7153.
[36] H. Li, C. Liu, J. Hao, A. Hirsch, Effect of addition of dendritic C_{60} amphiphiles on the structure of cationic surfactant solutions, J. Colloid Sci., 320 (2008) 307–314.
[37] H.X. Zhao, Q. Zou, S.K. Sun, C. Yu, X. Zhang, R.J. Li, Y.Y. Fu, Theranostic metal-organic framework core-shell composites for magnetic resonance imaging and drug delivery, Chem. Sci., 7 (2016) 5294–5301.
[38] Q. Chen, Q. He, M. Lv, Y. Xu, H. Yang, X. Liu, F. Wei, Selective adsorption of cationic dyes by UiO-66-NH_2, Appl. Surf. Sci., 327 (2015) 77–85.
[39] F. Ke, L.G. Qiu, J. Zhu, Fe_3O_4@MOF core-shell magnetic microspheres as excellent catalysts for the Claisen-Schmidt condensation reaction, Nanoscale, 6 (2014) 1596–1601.
[40] M. Zhao, Y. Sun, J. Lv, L. Cao, Y. Jiang, G. He, M. Zhang, Z. Sun, X. Chen, Enhanced photocatalytic performances of ZnO with Na doping and graphene oxide quantum dots, J. Mater. Sci. Mater. Electron., 27 (2016) 9131–9135.
[41] M. Kandiah, M.H. Nilsen, S. Usseglio, S. Jakobsen, U. Olsbye, M. Tilset, C. Larabi, E.A. Quadrelli, F. Bonino, K.P. Lillerud, Synthesis and stability of tagged UiO-66 Zr-MOFs, Chem. Mater., 22 (2010) 6632–6640.
[42] J.H. Cavka, S. Jakobsen, U. Olsbye, N. Guillou, C. Lamberti, S. Bordiga, K.P. Lillerud, A new zirconium inorganic building brick forming metal organic frameworks with exceptional stability, Chem. Soc., 130 (2008) 13850–13851.
[43] K.Y.A. Lin, Y.T. Liu, S.Y. Chen, Adsorption of fluoride to UiO-66-NH 2 in water: stability, kinetic, isotherm and thermodynamic studies, Colloid Interface Sci., 461 (2016) 79–87.
[44] S.M. Barrett, C. Wang, W. Lin, Oxygen sensing via phosphorescence quenching of doped metal–organic frameworks, J. Mater. Chem., 22 (2012) 10329–10334.
[45] J. Wang, W. Xu, L. Chen, X. Huang, J. Liu, Preparation and evaluation of magnetic nanoparticles impregnated chitosan beads for arsenic removal from water, Chem. Eng. J., 251 (2014) 25–34.
[46] C. Xiong, W. Wang, F. Tan, F. Luo, J. Chen, X. Qiao, Investigation on the efficiency and mechanism of Cd(II) and Pb(II) removal from aqueous solutions using MgO nanoparticles, Mater., 299 (2015) 664–674.
[47] B.C. Luo, L.Y. Yuan, Z.F. Chai, W.Q. Shi, Q. Tang, U(VI) capture from aqueous solution by highly porous and stable MOFs: UiO-66 and its amine derivative, Chem., 307 (2016) 269–276.
[48] A. Bhatnagar, W. Hogland, M. Marques, M. Sillanpää, An overview of the modification methods of activated carbon for its water treatment applications, Chem. Eng. J., 219 (2013) 499–511.
[49] Y.S. Ho, G. McKay, Pseudo-second order model for sorption processes, Process Biochem., 34 (1999) 451–465.
[50] J. Abdi, M. Vossoughi, N.M. Mahmoodi, I. Alemzadeh, Synthesis of metal-organic framework hybrid nanocomposites based on GO and CNT with high adsorption capacity for dye removal, Chem. Eng. J., 326 (2017) 1145–1158.
[51] Y. Ma, S.G. Wang, M. Fan, W.X. Gong, B.Y. Gao, Characteristics and defluoridation performance of granular activated carbons coated with manganese oxides, J. Hazard. Mater., 168 (2009) 1140–1146.
[52] Y. Zhan, J. Lin, J. Li, Preparation and characterization of surfactant-modified hydroxyapatite/zeolite composite and its adsorption behavior toward humic acid and copper(II), Envir. Sci. Pollut. Res. Int., 20 (2013) 2512–2526.
[53] Y. Song, K. Qu, C. Zhao, J. Ren, X. Qu, Graphene oxide: intrinsic peroxidase catalytic activity and its application to glucose detection, Mater., 22 (2010) 2206–2210.
[54] I. Langmuir, The adsorption of gases on plane surfaces of glass, mica and platinum, Chem. Phys., 40 (2015) 1361–1403.
[55] T.W. Weber, R.K. Chakravorti, Pore and solid diffusion models for fixed-bed adsorbers, AIChE J., 20 (1974) 228–238.
[56] G. Mckay, Adsorption of dyestuffs from aqueous solutions with activated carbon II: column studies and simplified design models, J. Chem. Technol. Biotechnol., 32 (1982) 773–780.
[57] Y. Hashimoto, K. Tokura, H. Kishi, W.M.J. Strachan, Prediction of seawater solubility of aromatic compounds, Chemosphere, 13 (1984) 881–888.
[58] N. Yin, K. Wang, L. Wang, Z. Li, Amino-functionalized MOFs combining ceramic membrane ultrafiltration for Pb (II) removal, Chem. Eng. J., 306 (2016) 619–628.
[59] D. Zhao, X. Yang, H. Zhang, C. Chen, X. Wang, Effect of environmental conditions on Pb(II) adsorption on β-MnO_2, Chem. Eng. J., 164 (2010) 49–55.
[60] S. Li, H. Bai, J. Wang, X. Jing, Q. Liu, M. Zhang, R. Chen, L. Liu, C. Jiao, In situ grown of nano-hydroxyapatite on magnetic CaAl-layered double hydroxides and its application in uranium removal, Chem. Eng., 193–194 (2012) 372–380.
[61] W. Sun, K. Yin, X. Yu, Effect of natural aquatic colloids on Cu(II) and Pb(II) adsorption by Al_2O_3 nanoparticles, Chem. Eng. J., 225 (2013) 464–473.
[62] L. Bo, Q. Li, Y. Wang, L. Gao, X. Hu, J. Yang, One-pot hydrothermal synthesis of thrust spherical Mg–Al layered double hydroxides/MnO_2 and adsorption for Pb(II) from aqueous solutions, Chem. Eng., J. 3 (2015) 1468–1475.
[63] N. Kannan, T. Veemaraj, Removal of lead(II) ions by adsorption onto bamboo dust and commercial activated carbons - a comparative study, J. Chem., 6 (2014) 247–256.

[64] M. Machida, M. Aikawa, H. Tatsumoto, Prediction of simultaneous adsorption of Cu(II) and Pb(II) onto activated carbon by conventional Langmuir type equations, J. Hazard. Mater., 120 (2005) 271–275.
[65] Faheem, H. Yu, J. Liu, J. Shen, X. Sun, J. Li, L. Wang, Preparation of MnO x -loaded biochar for Pb^{2+} removal: adsorption performance and possible mechanism, J. Taiwan Inst. Chem. Eng., 66 (2016) 313–320.
[66] Y. Wang, G. Ye, H. Chen, X. Hu, Z. Niu, S. Ma, Functionalized metal–organic framework as a new platform for efficient and selective removal of cadmium(II) from aqueous solution, J. Mater. Chemi. A, 3 (2015) 15292–15298.